Tellus
SERIES A
DYNAMIC
METEOROLOGY
AND OCEANOGRAPHY
PUBLISHED BY THE INTERNATIONAL METEOROLOGICAL INSTITUTE IN STOCKHOLM

*Tellus (2009), 61A, 498–511*

TELLUS

# On the selection of prognostic moments in parametrization schemes for drop sedimentation

*By* ULRIKE WACKER* and CHRISTOF LÜPKES, *Alfred–Wegener–Institut für Polar– und Meeresforschung, 27515 Bremerhaven, Germany*

(Manuscript received 24 October 2008; in final form 24 April 2009)

ABSTRACT

Common parametrization models for cloud microphysical processes use condensate mass density and/or particle number density as prognostic properties. However, other moments of the particle size distribution can likewise be chosen for prediction. This study deals with parametrization models with one and two, respectively, prognostic moments for the sedimentation of drop ensembles. The spectral resolving model defines the reference solution.

The evolution of the vertical profiles of liquid water content, drop number density and rain rate strongly depend on the choice of the prognostic moments in the parametrization models. In models with a single prognostic moment, its vertical profile is copied by all other moments. The moment of most physical pertinence is recommended for prediction. In models with two prognostic moments, the vertical profiles of all moments differ. The orders of the prognostic moments should be chosen close to the order of moments of highest relevance. Otherwise large errors occur. For example, comparison of modelled versus observed radar reflectivity (6th moment with respect to diameter) does not tell much about the quality of other properties if reflectivity is diagnosed from for example, number density and mass density. Furthermore, mass conservation is fulfilled only if mass density is forecasted.

## 1. Introduction

An adequate simulation of weather and climate should include clouds and precipitation, since they are important weather and climate parameters and influence many other processes in the troposphere and at the surface. However, in those models cloud microphysical processes are not treated in spectral resolving form, but their effects are described in parametrized form, based on the ideas presented by Kessler (1969), for the sake of computational efficiency. For instance, extensive schemes for mixed phase clouds are currently used in weather prediction models as COSMO of the Deutscher Wetterdienst (DWD; Doms et al., 2005) and as the one of the Japan Meteorological Agency (JMA; Saito et al., 2006) and in climate models as CCSM (NCAR; Collins et al., 2004) and ECHAM5 (MPI Hamburg; Roeckner et al., 2003). A spectral treatment of cloud microphysical processes is presently done in a weather forecast model for research purpose, see Lynn et al. (2005), and in cloud models, as for example, by Khain et al. (2004).

Parametrization schemes (or 'bulk schemes') for cloud microphysical processes are based on the assumption that the particle size distribution is well represented by a self-preserving drop size distribution with only few parameters. These parameters can be expressed in terms of few moments of the size distribution, such that the forecast of those moments is equivalent to the forecast of the spectrum. In the above mentioned weather and climate models, so-called 1-moment parametrization schemes are routinely used, in which only one moment of the spectrum of each category of condensate particles is forecasted. Any other moment of the spectrum is then diagnosed as a function of the single prognostic moment.

Schemes with two or more prognostic moments have been developed and applied to research models. 2-moment schemes generally used particle number density and condensate mass concentration as prognostic moments; examples are the schemes developed by Ferrier (1994) and by Seifert and Beheng (2005) for mixed phase clouds and by Lüpkes et al. (1989) for warm clouds. An example for a parametrization with three prognostic moments is the one reported by Milbrandt and Yau (2005b), who additionally forecast the radar reflectivity.

Information on the strengths and weaknesses of the parametrization approach can be gained from a comparison with the results from a microphysical spectral model ('reference model'), which is based on the solution of the prognostic equation for the hydrometer size distribution, for example, Lüpkes et al. (1989), Lynn and Khain (2007) and others. For an idealized system of a rain drop ensemble evolving under the influence of sedimentation alone, such a comparison is done by

*Corresponding author.
e-mail: Ulrike.Wacker@awi.de
DOI: 10.1111/j.1600-0870.2009.00405.x

Wacker and Seifert (2001), hereafter referred to as WS. The focus on sedimentation alone is certainly a strong restriction, when considering all processes, which modify a drop example, as for example, coagulation, evaporation and freezing. The simplified system has the advantage that the evolution of the drop size distribution and hence of the moments can be calculated analytically as function of space and time. This solution for the moments is a reference, against which the results from various parametrization models can be compared. WS used the liquid water content as prognostic moment for their 1-moment model. An important finding was that solutions from the parametrization model show a shock wave. This is in contrast to the reference solution and is explained by WS as follows. The reference solution accounts for gravitational sorting of the falling drops; that is the largest drops will arrive first at a particular height level, followed by the next drops in size. This feature cannot be reproduced by a 1-moment scheme, since the ensemble is shifted downward by its moment-weighted sedimentation speed. Furthermore, owing to the increase of the moment-weighted sedimentation velocity with increasing liquid water content, the sedimentation term in the prognostic equation of the liquid water content takes the form of a quasi-linear advection term. This term can cause solutions in form of shock waves. This solution type is hardly noticed in numerical solutions of the moment's equation, since the widely used numerical methods are diffusive and hence cover this effect. WS found shock waves to be also part of the solution of a 2-moment model with the prognostic variables liquid water content and drop number density; but here they play a weaker role, since some part of the gravitational sorting can be at least rudimentarily reproduced by the model. Therefore, the solution is closer to the result of the reference model than for the 1-moment model.

The different representation of the size sorting effect by different parametrization models is further investigated by Milbrandt and Yau (2005a). The evolution of the profiles of several moments of the particle ensemble matches the reference solution the better, the more moments are forecasted. They additionally show the influence of the assumed shape of the particle size distribution on the solution from the parametrization model, and suggest to diagnose a shape parameter of the distribution from current number and mass concentration.

Research on the appropriate treatment of sedimentation within parametrization schemes is ongoing. Geleyn et al. (2008), for instance, propose a refined 1-moment scheme for sedimentation by a statistical approach for the vertical distribution of liquid water within a model layer.

In this study, a central question concerns the dependence of the results of the bulk-parametrization approaches on the specific selection of the prognostic moments of the drop size distribution. This point has received little attention so far. Let $M_k$ denote the moment of order $k$ of the drop size distribution. In case of a 1-moment scheme with prognostic moment $M_k$, all moments $M_l$ of order $l \neq k$ are, if not prescribed, diagnosed from $M_k$, so that the spatial structure of $M_l$ is determined by that of $M_k$. Likewise for the 2-moment models it is not a priori obvious, how to choose the two prognostic moments $M_j$ and $M_k$, and how the results of $M_l$ will vary for different combinations.

This dependence will be elaborated in the present paper with the idealized model of a raindrop ensemble evolving under the influence of sedimentation, as in WS. The model differs from the one of WS insofar, as we consider here various candidates for the prognostic moments. It will be shown, how the resulting vertical profile of, for example, liquid water content depends on the choice of the prognostic moment(s).

Once the dependence of the results on the specific prognostic moments is found for the bulk models, the second central question arises, as to which moments are the most suitable ones to be predicted.

To concentrate on these two aspects, we specifically keep as close as possible to the framework of common bulk schemes, although some assumptions may be questioned, such as a self-preserving drop size distribution ranging for drop diameters $0 \leq D \leq \infty$ and a constant shape parameter of the assumed gamma distribution. An alternative concept is not within the scope of the present study.

In this paper, we start in Section 2 with the description of the spectral model for the evolution of the drop size distribution and the resulting reference solutions for the vertical profile of various moments. In Sections 3 and 4, the 1-moment and the 2-moment schemes, respectively, are investigated with regard to the dependence of the moments' profiles on the prognostic moment(s), and the profiles are compared with the reference solution. In Section 5, we will discuss the results and suggest criteria for the choice of the prognostic moments.

## 2. The moments' profiles as they follow from the spectral resolving microphysical model

The microphysical state of an ensemble of drops is characterized by the drop size distribution (DSD) $f(D, x, y, z, t)$ with $D$ denoting drop diameter, $x, y, z$ the spatial coordinates and $t$ time. $f(D, x, y, z, t)\,\mathrm{d}D$ gives the number of drops per unit volume in the diameter interval $[D, D + \mathrm{d}D]$. In the following we consider only sedimentation and discard any dependence on the horizontal coordinates $x, y$. The accordingly simplified budget equation for $f$ then takes the form

$$\frac{\partial f(D, z, t)}{\partial t} - \frac{\partial [v_T(D) f(D, z, t)]}{\partial z} = 0 \tag{1}$$

with the sedimentation velocity $v_T(D)$ of a drop with diameter $D$. As long as we assume that $v_T$ depends only on the drop size, eq. (1) is a strict linear PDE.

We adopt for the sedimentation velocity an empirical velocity–diameter relation in the form of a power law,

$$v_T(D) = \alpha D^{\beta}, \tag{2}$$

and use $\alpha = 1300\ \mathrm{cm}^{1/2}\ \mathrm{s}^{-1}$, $\beta = 0.5$ for raindrops (Kessler, 1969).

As outlined in WS, eq. (1) is solved by the method of characteristics for the given initial condition $f(D, z, t = 0) = f_0(D, z)$,

$$f(D, z, t) = f_0[D, z + v_T(D)t]. \tag{3}$$

That is, the number of drops in the interval d$D$ at height $z$ and time $t$, $f(D, z, t)\,\mathrm{d}D$, is equal to the initial number of drops in the interval d$D$ at height $z + v_T(D)t$ with $v_T(D)\,t$ being the distance, which drops of diameter $D$ have travelled during time $t$.

The initial vertical profile is now prescribed as in WS in form of a homogeneous cloud layer with upper and lower boundaries at heights $z_u$ and $z_l$, respectively:

$$f_0(D, z) = \begin{cases} f_0(D) & \text{for } z_l \le z \le z_u \\ 0 & \text{else} \end{cases} \tag{4}$$

The solution $f(D, z, t)$ of (1) as given in (3) in combination with (2) and (4) follows as (see WS)

$$f(D, z, t) = \begin{cases} f_0(D) & \text{for } D_l(z, t) \le D \le D_u(z, t) \\ & \text{and } z \le z_u \\ 0 & \text{else} \end{cases} \tag{5}$$

with $D_l$ and $D_u$ denoting

$$D_l = \begin{cases} \left(\frac{1}{\alpha}\frac{z_l - z}{t}\right)^{\frac{1}{\beta}} & \text{for } z \le z_l \\ 0 & \text{for } z > z_l \end{cases}$$

$$D_u = \begin{cases} \left(\frac{1}{\alpha}\frac{z_u - z}{t}\right)^{\frac{1}{\beta}} & \text{for } z \le z_u \\ 0 & \text{for } z > z_u. \end{cases} \tag{5}$$

$D_l$ is the diameter of the smallest drop which, after starting at level $z_l$, has arrived at level $z$ after time $t$; and $D_u$ is the diameter of the largest drop which, after starting at level $z_u$, has arrived at level $z$ after time $t$. Both $D_u$ and $D_l$ decrease with increasing time.

The $k$th moment $M_k$ of a DSD is defined as

$$M_k(z, t) = \int_0^\infty D^k f(D, z, t)\,\mathrm{d}D. \tag{6}$$

The 0th moment is the number density of drops, $M_0 = N$, the third moment $M_3$ is proportional to the liquid water content, $L = M_3 \pi \rho_w / 6$ ($\rho_w$: bulk density of liquid water) and the 6th moment $M_6$ is the radar reflectivity, provided the particles are assumed spherical. Once $f(D, z, t)$ is known, one can calculate the evolution of the various moments from (6).

We now choose as DSD for rain drops a gamma distribution as in Milbrandt and Yau (2005a)

$$f_0(D) = n_0 D^\mu \exp(-\lambda D) \tag{7}$$

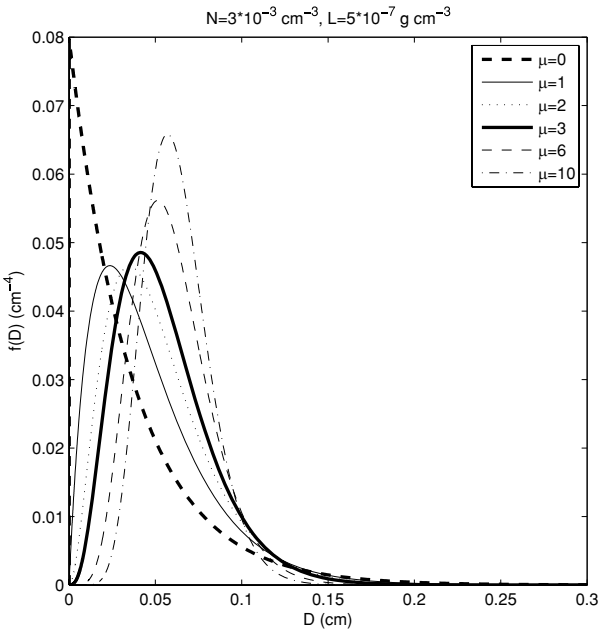


*Fig. 1.* Drop size distribution function $f(D)$ in form of a gamma-function (7) as function of drop diameter $D$ for number concentration $N = 3 \times 10^{-3}\ \mathrm{cm}^{-3}$, liquid water concentration $L = 5 \times 10^{-7}$ g $\mathrm{cm}^{-3}$, and various parameter values $\mu$.

with the three parameters $n_0$, $\mu$ and $\lambda$. The exponent $\mu$ is a shape parameter. For $\mu = 0$, $f_0(D)$ takes the form of the Marshall–Palmer size distribution, which is frequently assumed for raindrop ensembles in parametrization schemes, for example, Kessler (1969). Milbrandt and Yau (2005a) suggest the use of $\mu = 3$. In Fig. 1, the size distribution is plotted for various values of $\mu$, but for the same number concentration $N$ and liquid water content $L$. The influence of $\mu$ is such that the size distribution becomes narrower with increasing $\mu$.

Figure 2 gives an example for the development of the moments' profiles for the initial homogeneous cloud layer according to (4) and (7). As expected, the signals move downward under the impact of sedimentation. Due to gravitational sorting, the signals' shapes are deformed, that is the initial discontinuities at the upper and lower boundaries of the signal are smoothed and the maxima are damped. The signals of the higher moments travel faster, since they are influenced more strongly by the larger, faster falling drops. The two examples in Fig. 2 differ due to the chosen shape parameter $\mu$. As the size distribution becomes narrower with increasing $\mu$ (see Fig. 1), the moments become dominated by drops of similar sizes, such that the downward shifts of the various moments converge. In the limiting case $\mu \to \infty$, all drops and any moments would settle at the same fall speed, since the DSD becomes essentially monodispersed.

The evolution of a moment $M_k(z, t)$ can be calculated in two ways. First, as done before, one solves eq. (1) for the DSD and then uses the definition of $M_k$ by (6). Alternatively, the

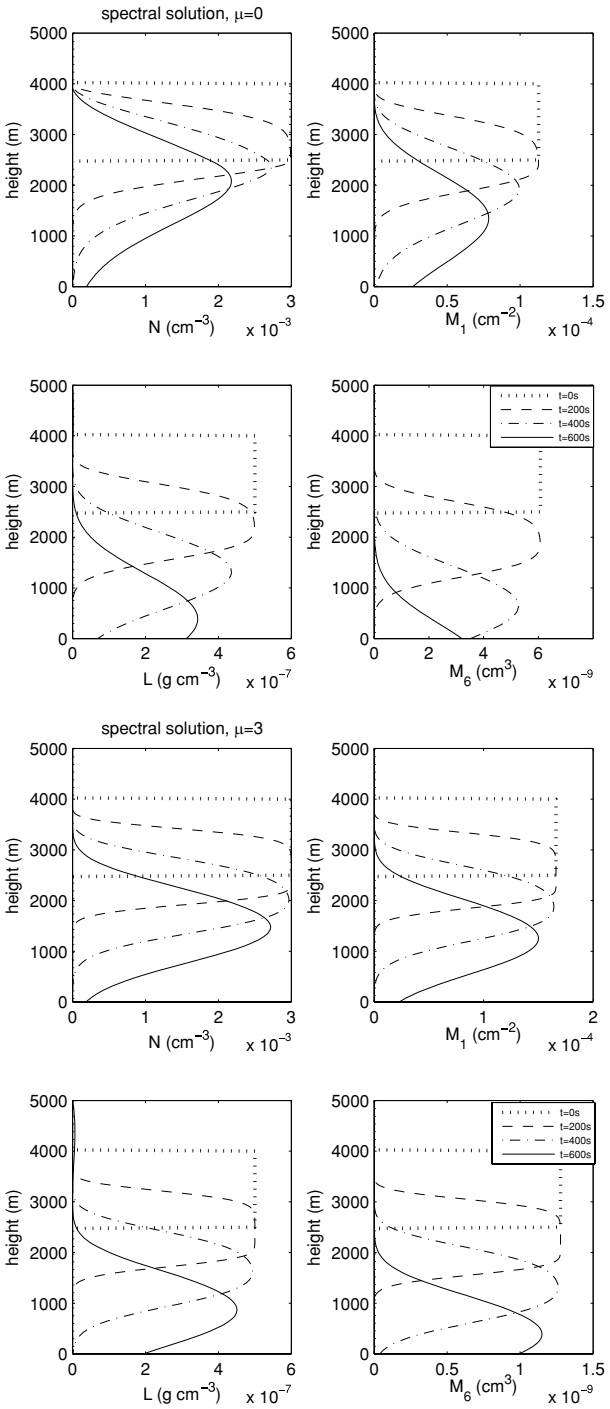


*Fig. 2.* Evolution of the vertical profiles of four moments of the drop size distribution (7) with $\mu = 0$ (first two rows) and $\mu = 3$ (last two rows) as follows from the spectral reference model (solution of (1)). Initial conditions are defined by prescribing $N(z, t = 0)$ and $L(z, t = 0)$ as in Fig. 1.

prognostic equation for $M_k$ is derived from the budget equation (1), multiplied with $D^k$ and integrated over the drop ensemble. The result is

$$\frac{\partial M_k}{\partial t} - \frac{\partial F_k}{\partial z} = 0 \tag{8}$$

$F_k = \int_0^\infty v_T(D) D^k f(D, z, t) \mathrm{d}D$ denotes the sedimentation flux for the $k$th moment.

Equation (8) is a source-free budget equation for any moment $M_k$. The volume integral $\int_V M_k \mathrm{d}V$ changes only by fluxes $F_k$ into and out of that volume, which gives a straightforward conservation condition. This reads for horizontally homogeneous conditions

$$\int_0^\infty M_k(z, t)\,\mathrm{d}z + \int_0^t F_k(z = 0, t')\,\mathrm{d}t' = C_k = \text{const.} \tag{9}$$

It is relevant for the following Sections 3 and 4, that the sedimentation flux $F_k$ cannot be expressed as function of the prognostic $M_k$ alone, except in the special case that the sedimentation velocity $v_T$ is independent of drop size, that is $\beta = 0$ in (2). Hence, in the general case, eq. (8) cannot be solved alone. Either its solution requires knowledge of the DSD; but then $M_k$ simply follows from (1) and the solution of (8) is not required. Otherwise, the flux $F_k$ has to be parametrized, that is $F_k$ has to be expressed in terms of the prognostic moment(s), for which a budget equation as (8) is to be solved.

Familiar parametrization models as will be used in this study, are based on the assumption of a self-preserving rain drop size distribution of the type (7). The knowledge of the parameters as function of space and time is then equivalent to the knowledge of the DSD. The free parameters can be uniquely expressed by the same number of moments, thus solving the coupled system of budget equations for those moments will likewise allow the reconstruction of the DSD. In difference to the spectral model, in which the DSD becomes naturally truncated due to gravitational sorting, see the solution (5), the integration boundaries are always set to $D = 0, \infty$ in the parametrization model. This restriction might be skipped in favour of time dependent integration boundaries in case of the present idealized sedimentation model. But since this is not feasible when other cloud physical processes are included, we will neither do here.

Frequently it is assumed in parametrization schemes, that only one or two moments of the DSD (7) vary independently. Then additionally two or one, respectively, closure assumptions are required to determine all three parameters and the DSD.

## 3. The 1-moment scheme

In 1-moment parametrization schemes, only a single moment $M_k$ is forecasted. We will study in this section the influence of the choice of this particular $k$th moment on the resulting evolution of the vertical profile of, for example, the 0th, the 3rd and the 6th moment. It is assumed that the drop size distribution is always of the form (7). Two closure conditions are necessary. We choose

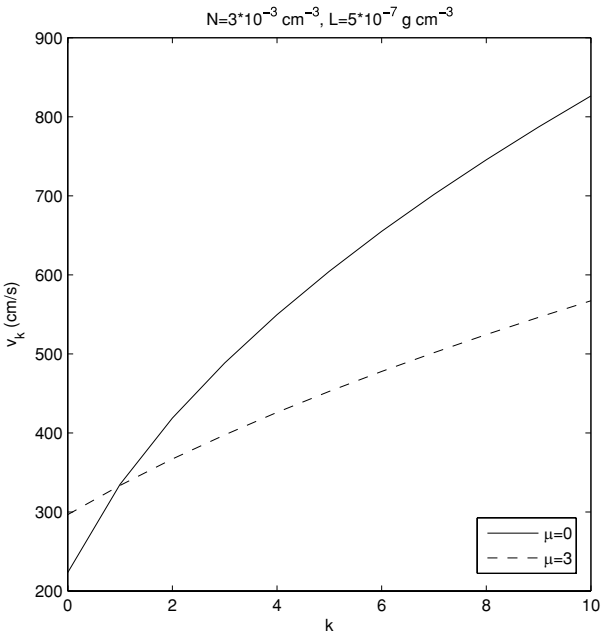


*Fig. 3.* Moment-weighted sedimentation velocity $\overline{v}_k$ according to (A5) as function of $k$ for a drop size distribution (7) with $\mu = 0$ and $\mu = 3$, respectively, and conditions for $N$ and $L$ as in Fig. 1.

the common approach $n_0 = \text{const.}$ and $\mu = \text{const.}$, yet other closure conditions are feasible. The sedimentation flux $F_k$ and the moment-weighted sedimentation velocity $\overline{v}_k = F_k/M_k$ are expressed as functions of the moment $M_k$ alone. The equations for $F_k(M_k)$ and $\overline{v}_k(M_k)$ are given in (A4) and (A5) in Appendix A.

We first inspect the moment-weighted sedimentation velocity $\overline{v}_k$ (eq. A5). $\overline{v}_k$ depends on the order $k$ of the prognostic moment. This is illustrated by an example. We select a constant $\mu$, we assume the same values for $N$ and $L$ as in Fig. 1, and we calculate the parameters $n_0$ and $\lambda$ to get the drop size distribution. For this DSD we calculate $\overline{v}_k$ for $k = 0, 1, \ldots 10$. As illustrated in Fig. 3, $\overline{v}_k$ increases with increasing $k$ due to the increasing contribution of large, fast falling drops on $\overline{v}_k$. Furthermore, since the size distribution becomes narrower with increasing $\mu$, see Fig. 1, the range of variation of the moment-weighted velocity decreases accordingly. Indeed, $\overline{v}_k$ varies roughly by a factor 4 if $\mu = 0$ and only by a factor 2 if $\mu = 3$ in the examples presented in Fig. 3.

We now turn to the budget equation (8) for $M_k$. Due to $F_k = F_k(M_k)$ in the 1-moment parametrization, we can rewrite this equation in the form of an advection equation

$$\frac{\partial M_k}{\partial t} - \tilde{v}_k \frac{\partial M_k}{\partial z} = 0 \tag{10}$$

with the apparent advection velocity

$$\tilde{v}_k = \frac{\mathrm{d}F_k}{\mathrm{d}M_k} = \frac{\beta + k + \mu + 1}{k + \mu + 1}\,\overline{v}_k \;>\; \overline{v}_k\,. \tag{11}$$

The PDE (10) is of the mathematical type of a quasi-linear source-free advection equation and describes the propagation of the signal $M_k(t, z)$ with the velocity $\tilde{v}_k = \tilde{v}_k(M_k)$ depending on the signal $M_k$ itself. In contrast to eq. (10), eq. (1) for $f(D)$ is a strict-linear advection equation, since the advection velocity is independent of the variable $f$.

WS discuss eq. (10) for the case that $M_k$ is replaced by the liquid water mass concentration $L\,(\propto M_3)$. They solve the PDE (10) analytically for given initial conditions, and they document that the dependency of $\tilde{v}_k$ on $M_k$ can lead to shock-wave solutions.

Here, emphasis is put on the impact of the selected prognostic moment. Suppose that $M_k$ is chosen as the relevant moment. Then the apparent advection velocity $\tilde{v}_k$ determines the propagation of $M_k$. Any other moment $M_l$ ($l \neq k$) can be expressed in terms of $M_k$, see eq. (A7). Once $M_k(z, t)$ is known as solution of (10), the distribution $M_l(z, t)$ is determined as $M_l[M_k(z, t)]$, thus it will have the same spatial and temporal structure as $M_k(z, t)$ regulated by $\tilde{v}_k$. The moment-weighted sedimentation velocities $\overline{v}_k$, $\overline{v}_l$ differ for $k \neq l$, see Fig. 3, and so will the apparent advection velocities $\tilde{v}_k$, $\tilde{v}_l$, see eq. (11). They are ordered in size according to the sequence (see eq. A11)

$$\tilde{v}_l = \left\{ \begin{array}{c} < \\ = \\ > \end{array} \right\} \tilde{v}_k \quad \text{for} \quad l = \left\{ \begin{array}{c} < \\ = \\ > \end{array} \right\} k. \tag{12}$$

Thus the higher the order of the selected prognostic moment is, the faster propagates the signal, and this propagation speed is reflected in the evolution of the profile of each moment diagnosed from the prognostic one. Consequently, if we select instead $M_l$ ($l \neq k$) as the relevant prognostic moment, the advection velocity $\tilde{v}_l$ determines the propagation of $M_l$, and we find a solution $M_l(z, t)$, which differs from $M_l[M_k(z, t)]$.

Equation (10) is solved numerically by a MUSCL-Hancock scheme (Toro, 1999). Figure 4 gives examples for the evolution of the profiles of various moments for the special cases that either the 0th moment (number concentration $N$), the 3rd moment (proportional to the liquid water mass concentration $L$) or the 6th moment (radar reflectivity) is chosen as prognostic moment. For comparison, also the reference solution of the spectral model is plotted. The initial conditions are the same as used for Fig. 2. The parameters $n_0$ and $\lambda$ are calculated from the initial conditions for $N(t = 0)$ and $L(t = 0)$ for $z_l \leq z \leq z_u$ as used for Fig. 2, from which follows the initial state for any moment $M_k$. $n_0$ is kept constant later on.

The solution from the 1-moment model always shows a shock wave on the leading edge of the signal, due to the initial discontinuity. A rarefaction wave develops in the rear of the signal; see the discussion in WS for the $L$-profile.

For the case that $M_0$ is the prognostic moment ('$M_0$-model'), the maxima of $N\,(=M_0)$, $L\,(\propto M_3)$ and $M_6$ after a given integration time are found at the same height, as to be expected from the diagnosis $L = L(M_0)$ and $M_6 = M_6(M_0)$. The same is true when

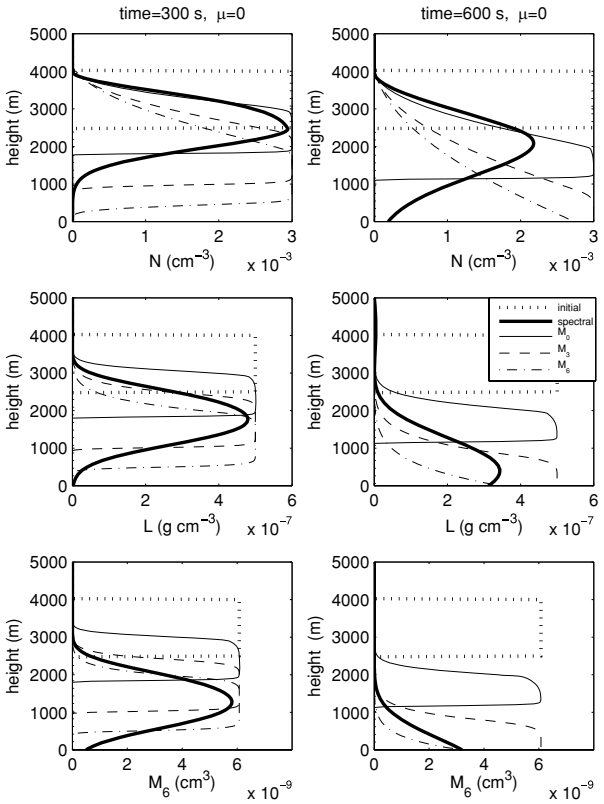


*Fig. 4.* Vertical profiles of the number density $N$, the liquid water concentration $L$, and the 6th moment $M_6$ (radar reflectivity), valid at $t = 300$ s and at $t = 600$ s, obtained from the reference spectral model and from the 1-moment model for prognostic moments $M_0$, $M_3$ and $M_6$, respectively. Shape parameter of the drop size distribution (7) is $\mu = 0$. Initial conditions for $N$ and $L$ are as in Fig. 1.

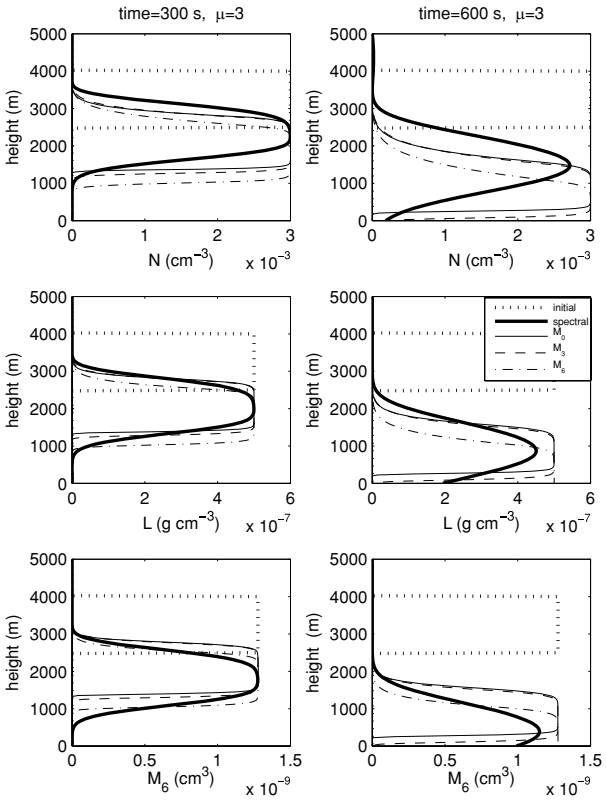


*Fig. 5.* As Fig. 4, but for the shape parameter $\mu = 3$.

$M_3$ or $M_6$ is the prognostic moment ('$M_3$-model', '$M_6$-model'). The heights of the maxima in the $M_0$-, $M_3$- and $M_6$-models, however, differ. The maximum is found in the $M_3$-model further downward, see for example, eq. (A10) for $\overline{v}_3 > \overline{v}_0$. In the $M_6$-model, the signal propagates still faster. In the reference model, however, different moments propagate at different velocities, and hence the maxima of $N$, $L$ and $M_6$ are always found at different heights at time $t$.

Major features are similar, when the shape parameter $\mu = 3$ is chosen (Fig. 5). But due to the narrower DSD (Fig. 1) the moment-weighted sedimentation speeds (Fig. 3) do not differ as strong as in the case $\mu = 0$, hence the resulting profiles from the various models are closer. Vice versa, we can expect the largest differences between the results of the bulk models with different prognostic moments in the $\mu = 0$-case due to the broadest DSD.

The evolution of the vertical profile from the various bulk models and the reference model show better agreement, when the moment of most interest is forecasted. For example, the $N$-profile is best reproduced by the $M_0$-model. Furthermore, the agreement is better for $\mu = 3$ than for $\mu = 0$. Very large drops are always present in the DSD presumed in the bulk model, and they influence the moment-weighted sedimentation velocity. This influence increases with increasing order of the forecasted moment, and one should tend in case of indecision rather towards the forecast of a low order moment.

## 4. The 2-moment scheme

2-moment parametrization schemes have the advantage over 1-moment schemes, that they allow to account for many more processes, which influence the drop ensemble and that a self-preserving distribution like (7) can be reconstructed in terms of two parameters, most frequently $n_0$ and $\lambda$, while $\mu$ is again fixed. These two parameters then follow by the solution of the budget equations for any combination of two moments $M_j$ as well as $M_k$, for example, the 0th and the 3rd moment.

We select $M_j$ and $M_k$ as the relevant ones ('$M_jM_k$-model'). Their budget equations (see 8) read

$$\frac{\partial M_j}{\partial t} - \frac{\partial F_j(M_j, M_k)}{\partial z} = 0 \tag{13}$$

$$\frac{\partial M_k}{\partial t} - \frac{\partial F_k(M_j, M_k)}{\partial z} = 0. \tag{14}$$

Each of the sedimentation fluxes $F_j$ and $F_k$ is a function of both moments $M_j$ and $M_k$, given in (B3) and (B4) in Appendix B.

We assume $j < k$ everywhere. Once $j$ and $k$ are fixed, any other moment $M_l$ follows diagnostically as $M_l(t, z) = M_l[M_j(t, z), M_k(t, z)]$ and no longer from a budget equation.

The moment-weighted sedimentation velocity $\overline{v}_k$ depends on the order $k$ and on $\lambda$, see eq. (B6). For prescribed values $N$ and $L$, the parameter $\lambda$ is fixed, and the same result is found for $\overline{v}_k$ as in the 1-moment model (Fig. 3). The increase of the moment-weighted sedimentation velocity $\overline{v}_k$ with $k$ is expected to influence the evolution of the moments' profiles as follows from solution of prognostic eqs (13) and (14), however, in a different way as in the 1-moment model due to the dependence $\lambda = \lambda(M_j, M_k)$.

Equations (13) and (14) form a coupled set of PDEs. As discussed in WS for the $M_0M_3$-model, they can be cast into a set of quasi-linear PDEs, and the solutions allow for shock waves. Equations (B3) and (B4) are solved numerically by the same MUSCL-Hancock scheme as used for solving eq. (10) in Section 3.

Figure 6 shows the results for the vertical profiles of the number concentration $N$ and the liquid water concentration $L$ as follow from the 2-moment model after 300 s and after 600 s integration time for the cases that (i) $M_0$ and $M_3$ and (ii) $M_0$ and $M_6$ are selected as the prognostic moments. The results from the reference model are again shown as comparison. The shape parameter is set $\mu = 0$.

The simulated profiles of the number density $N$ ($=M_0$) from the $M_0M_3$- and $M_0M_6$-models, for which $M_0$ is a prognostic moment ($j = 0$), are close to each other, but obviously different. They are in overall agreement with the reference solution, although both models give a faster downward shift.

In the $M_0M_3$-model results, matters are similar for the liquid water content $L$ ($\propto M_3$) as for $N$, except that the downward propagation of the $L$-maximum is slightly retarded and that the maximum is damped after 600 s in the $M_0M_3$-model as compared to the reference model results. Furthermore, a considerable amount of $L$ reaches $z = 0$ earlier in the bulk model than in the spectral model. Regarding the profile of $M_6$, the $M_0M_3$-model gives totally unrealistic results. The plotted $M_6$-values have been divided by 100 in Fig. 6. The order $l = 6$ is larger than the highest order $k = 3$ of a prognostic moment in the $M_0M_3$-model; according to eq. (B8) with $j = 0,\ k = 3,\ l = 6$, it holds $M_6 \propto M_3^2 M_0^{-1}$. Since the $M_0$-signal moves downward more slowly than the $M_3$-signal, $M_0$-values are small at low altitudes, which brings about the excessive $M_6$-values. Such a feature may cause huge problems, when for example, the 6th moment is diagnosed from this $M_0M_3$-model and is compared with observed radar reflectivity for verification purposes. This is not a shortcoming of the $M_0M_3$-model as long as the goal of the NWP or climate model is to provide information on $L$ and $N$, but this demonstrates the limited information gained from a comparison of the diagnosed moment $M_6$ with observed radar reflectivity.

The $M_0M_6$-model results show a different feature after 300 s simulation time: $M_6$ is in reasonable agreement with the reference solution. The $L$-profile comes out as a narrow signal after 300 s with a peak at about 2000 m height and as a weak signal after 600 s, suggesting that water mass has been lost. In this model the evolution of $M_3$ (and hence $L$) is not controlled anymore by a budget equation as for $M_0$ and $M_6$, but diagnosed from the prognostic moments using eq. (B8). $M_6$ is the highest prognostic moment ($k = 6$). According to (B8) we find for $l = 3$ (thus $j < l < k$) that $M_3 \propto M_0^{1/2} M_6^{1/2}$, and $M_3$ is expected to be low whenever $M_0$ or $M_6$ are low. The maxima in the $M_6$-profiles from all models have already left the region of consideration after 600 s simulation time.

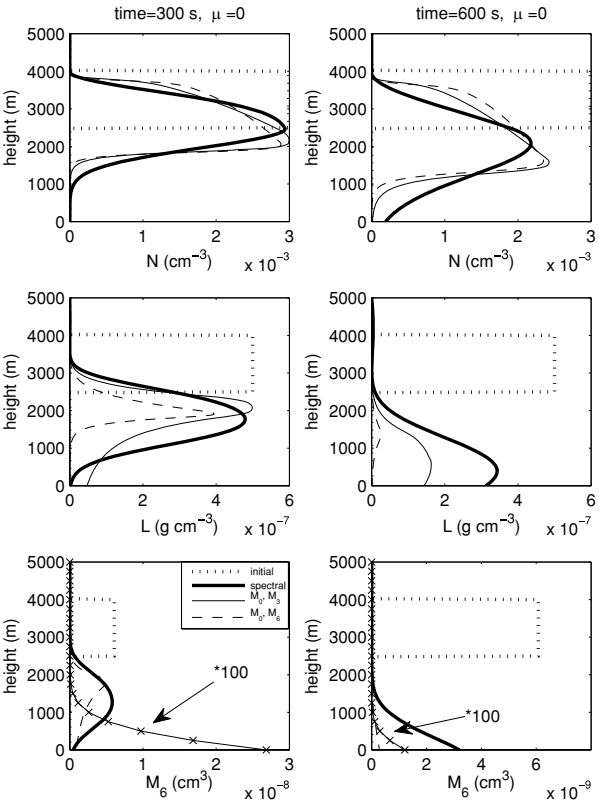


*Fig. 6.* Vertical profiles of the number density $N$, the liquid water concentration $L$, and the 6th moment $M_6$ (radar reflectivity) valid at $t =$ 300 s and at $t = 600$ s as follow from the reference spectral model and from the 2-moment scheme with $M_0$, $M_3$ and $M_0$, $M_6$, respectively, as prognostic moments. Shape parameter of the drop size distribution (7) is $\mu = 0$. Initial conditions for $N$ and $L$ are as in Fig. 1. Note that the $M_6$-values for the $M_0M_3$-model (marked with $\times$) are to be multiplied by 100.

We discuss now some other combinations of $M_j$, $M_k$ as prognostic moments for the same initial conditions $N(z, t = 0)$ and $L(z, t = 0)$ as used in Fig. 6. Fig. 7 shows the profiles of $N$, $L$ and $M_6$ after 300 s integration time. $j$, $k$ are chosen to be within 0 and 3 (left-hand column) and to be somewhat extreme with $k > 3$ (right-hand column). Some of the profiles $N$, $L$ and $M_6$ show values, which considerably exceed the maximum initial

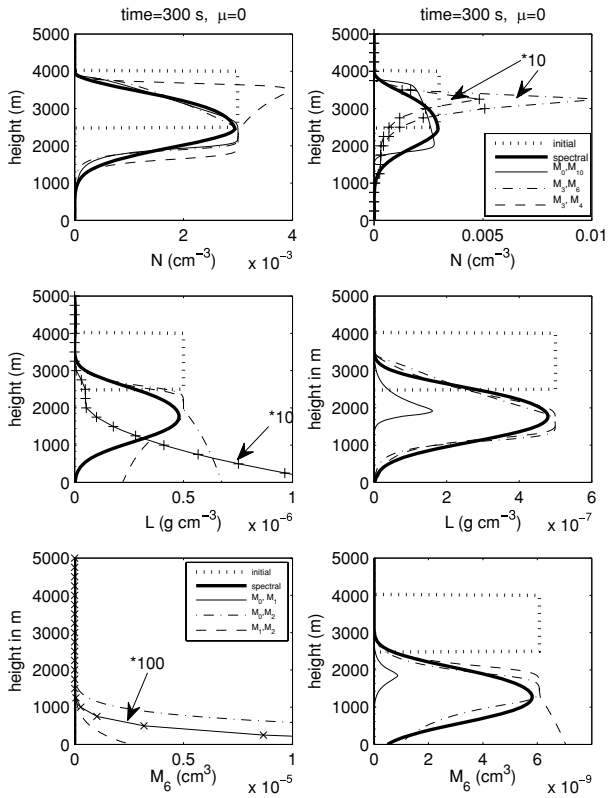


*Fig. 7.* As Fig. 6, but for other combinations of prognostic moments. Results are valid at $t = 300$ s. Note that the $N$-values for the $M_3M_6$- and $M_3M_4$-models and $L$-values for the $M_0M_1$-model are to be multiplied by 10 ('+'), and that the $M_6$-values for the $M_0M_1$-model are to be multiplied by 100 ('×'), and that the scaling of the abscissae differs from that of the previous figures.

values, similarly to the $M_6$-profile in the $M_0M_3$-model (Fig. 6) discussed above. As an example, such an overshooting is seen in the reconstructed profile of the 0th moment ($l = 0$) in the $M_3M_6$- and $M_3M_4$-models. We compare these diagnosed $M_0$-profiles with the predicted $M_0$-profiles from the $M_0M_1$-, $M_0M_2$-, $M_0M_3$-models etc., in which $M_0$ is a prognostic moment: The overshooting in the diagnosed $M_0$-profiles are located at the upper flank of the predicted $M_0$-profiles. This feature is henceforth referred to as an 'overshooting at the upper flank' (of the predicted signal) for shortness. Overshooting is also seen in the diagnosed profiles of $M_6$ ($l = 6$) in the $M_0M_1$-, $M_0M_2$-, $M_1M_2$- and $M_3M_4$-models. Compared to the profile $M_6$ from the $M_3M_6$-model, the overshooting is located at the lower flank of the predicted signal.

In general, the tendency to overestimate a diagnostic moment $M_l$ is expected, whenever $M_l$ is reconstructed from $M_j$ and $M_k$ for either $l < j, k$ or $l > j, k$. The overshooting occurs for $l < j, k$ ($l > j, k$) on the upper (lower) side of the predicted signal. The reason for the overshooting of the diagnosed $M_l$-profile is, that the $M_k$-signal propagates faster downward than the $M_j$-signal for $j < k$. According to eq. (B8), $M_l \propto [\, M_j^{k-l}/M_k^{j-l}]^{1/(k-j)}$ for $l < j, k$, hence we expect large values of the diagnosed $M_l$, whenever $M_k$ (but not $M_j$) becomes very small, that is at upper height. For $j, k < l$, matters are inverted. According to eq. (B8), we find $M_l \propto [M_k^{l-j}/M_j^{l-k}]^{1/(k-j)}$, and we expect large $M_l$, where $M_j$ decreases faster than $M_k$, that is at lower height. The overshooting is the stronger, the larger is the deviation between the moments' orders $l$ and $j$, and $l$ and $k$, respectively.

Matters are different for $j < l < k$, see for example in Fig. 7 the profiles $L$ and $M_6$ from the $M_0M_{10}$-model, that is for $l = 3$ and 6, $j = 0$, $k = 10$. Equation (B8) tells that $M_l \propto [M_k^{l-j}M_j^{k-l}]^{1/(k-j)}$ for $j < l < k$, and no excessive values show up in the diagnosed profiles. Yet either small $M_j$ or $M_k$ causes low values of $M_l$. The agreement between the spatial structure of the reconstructed profile of $M_l$ and that of the solution from the reference model is not bad, but the maximum can be strongly damped; the agreement is better when $l$ is close to $j$ or $k$.

These findings suggest to choose the prognostic moments $M_j$ and $M_k$ such that it gives the smallest range of $j$ and $k$ to embrace the required moments $M_l$ in the forecast model. It is explicitly mentioned that a condition $j \le l \le k$ cannot be achieved as long as $\beta > 0$, because the sedimentation flux is proportional to a higher order moment, $F_k \propto M_l$ with $l = k + \beta$, see eqs (B3) and (B4). The selection of the prognostic moment of order $k + \beta$ is no remedy, because the forecast of $M_{k+\beta}$ would require the flux $F_{k+\beta}$ which in return is proportional to the higher order moment $M_{k+2\beta}$. When other cloud microphysical processes are to be included, their parametrization equations are proportional to moments of order $l'$, and $l'$ may be likewise outside the range between $j$ and $k$.

We now turn to the shock wave as part of the solution of the PDEs (13) and (14). The shock wave travels at the leading edge of the signal, as discussed in WS. It propagates very fast (and fastest for small $j$, $k$) and quickly transmits information of the propagating signal. In all the examples presented in Figs. 6 and 7, the shock wave has already passed the level $z = 0$ after 300 s simulation time.

The amplitude of the shock wave depends on the minimum values $N_{\min}$ and $L_{\min}$, which have to be introduced to avoid mathematical singularities, see Appendix B. $N_{\min}$ and $L_{\min}$ can be freely chosen, so that some ambiguity enters the solution. The propagation speed of the shock wave decreases with increasing $N_{\min}$ at fixed $L_{\min}$, that is with decreasing average drop mass. Once the shock wave has reached the level $z = 0$, the vertical profiles of the moments are independent of the chosen $N_{\min}$- and $L_{\min}$-values. Thus their choice is important during the very early phase and unimportant for later times. In the examples discussed in this section, the shock wave passes the level $z = 0$ within less than 100 s.

The initial phase may be of relevance for the time series of the precipitation rate $RR$ at the surface, here defined as $z = 0$. $RR = F_3\,\pi\,\rho_w/6$ is the total mass flux with $F_3$ denoting the sedimentation flux of the 3rd moment according to eq. (A3)

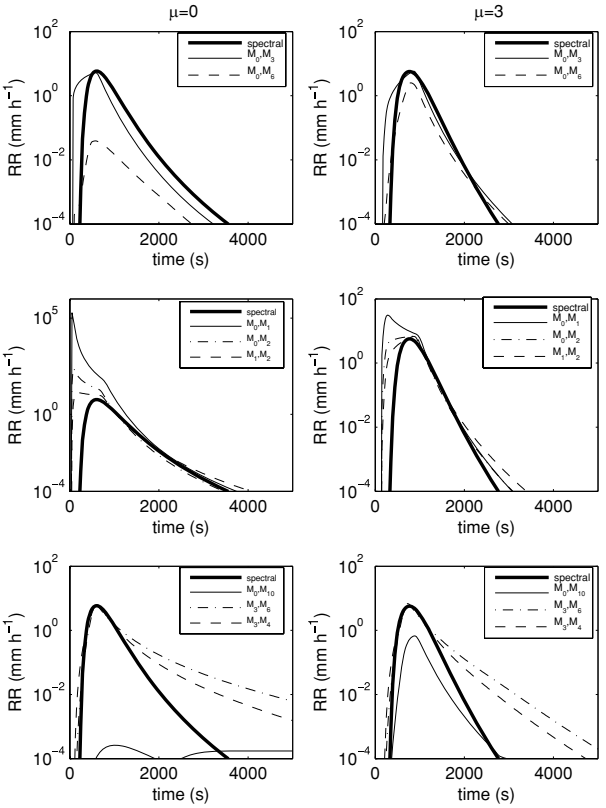


*Fig. 8.* Time series of precipitation rate $RR$ at $z = 0$ for the reference spectral model (thick line) and various 2-moment models as used in Figs. 6 and 7 for $\mu = 0$ (left-hand column) and for $\mu = 3$ (right-hand column). The ordinate is scaled logarithmically.

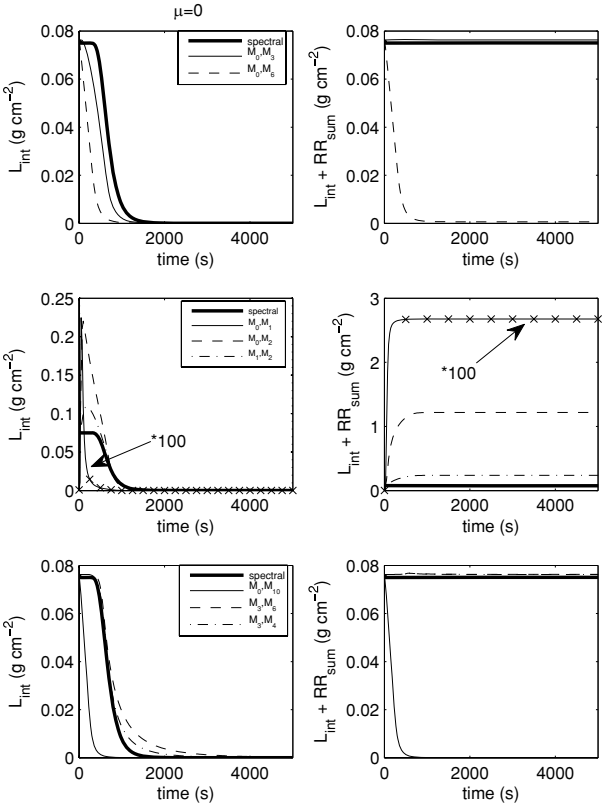


*Fig. 9.* Time series of vertically integrated liquid water content (left-hand column) and of the sum of vertically integrated liquid water content and accumulated rain at surface (right-hand column). Results follow from the spectral model (thick line) and from various 2-moment models as used in Figs. 6 and 7 for $\mu = 0$. Note that the $L_{\rm int}$- and ($L_{\rm int} + RR_{\rm sum}$)-values from the $M_0M_1$-model are to be multiplied by 100 ('×').

in general or according to (B9) for the 2-moment model. In Fig. 8, the time-series of $RR$ (converted to the unit mm h$^{-1}$; logarithmic scaling) are shown in the left-hand column for the results following from the reference model (thick line) and from various 2-moment models, as used before in Figs. 6 and 7 for $\mu = 0$. The onset of precipitation is mostly earlier in the results from the parametrization models than in those from the reference model, and the precipitation rates in the initial phase often exceed those from the reference solution. Both features are related to the passage of the fast travelling shock wave in the solution for the prognostic moments $M_j$, $M_k$, from which $RR$ is diagnosed. $RR$ as well as the flux $F_3$ are proportional to the moment of order $3 + \beta$, see (A4) and (2), with $\beta$ denoting the exponent in the equation of the terminal velocity. So we can apply a discussion of the evolution of the vertical profile for $RR$ or $F_3$ similar to the discussion for a diagnosed moment $M_l$ of order $l = 3 + \beta$. Hence we expect in the lower part of the profile of the flux $F_3 = F_3(M_j, M_k)$ overestimated values if $j, k < 3 + \beta$. When they arrive at $z = 0$, they give peak values in the time series of $RR(t)$, as seen in Fig. 8 (left middle figure). If the initial phase is discarded from interpretation, we find a reasonable agreement between the results from the 2-moment models and the reference model, if $j$ and/or $k$ are close to $3+\beta$, that is for the $M_3M_4$-, the $M_3M_6$- and eventually the $M_0M_3$-models for the cases in Fig. 8. Otherwise the results strongly distinguish from each other.

An important aspect in modelling is the conservation of total $H_2O$-mass. In our pure-sedimentation model this condition is simply stated by $L_{\rm int} + RR_{\rm sum} = $ const. with $L_{\rm int}$ denoting the vertically integrated liquid water content and $RR_{\rm sum}$ denoting the accumulated rain flux at $z = 0$, as follows from eqs (8) and (9) for $k = 3$. In Fig. 9, $L_{\rm int}$ and the sum of $L_{\rm int}$ and $RR_{\rm sum}$ are plotted as function of time for various combinations of prognostic moments $M_j$ and $M_k$. In those models with $M_3$ as prognostic moment, mass conservation is fulfilled, since (8) for $k = 3$ controls the mass budget. Generally, if $M_j$ and $M_k$ are forecasted, then $C_j$ and $C_k$ are conserved, see eq. (9). The numerical results fulfil this criterion (not shown here). If, however, $M_3$ is not among the prognostic moments, then mass conservation is no longer ensured. We take the $M_0M_6$-model as an example. As seen in Fig. 9, $L_{\rm int} + RR_{\rm sum} = $ const. decreases with time. This is a consequence of the diagnosis of the moment $M_3$ (hence $L$) and

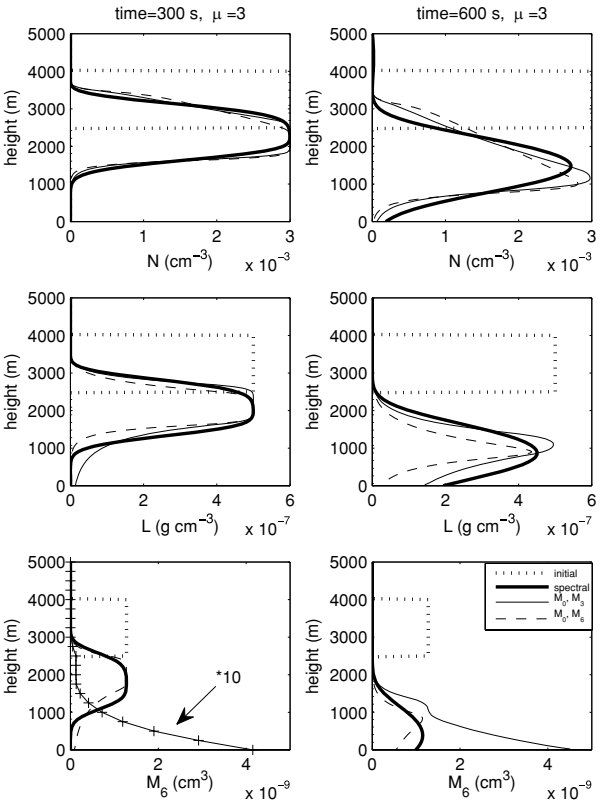


*Fig. 10.* As Fig. 6 but for $\mu = 3$. Note that the $M_6$-values for the $M_0M_3$-model at $t = 300$ s are to be multiplied by 10 ('+').

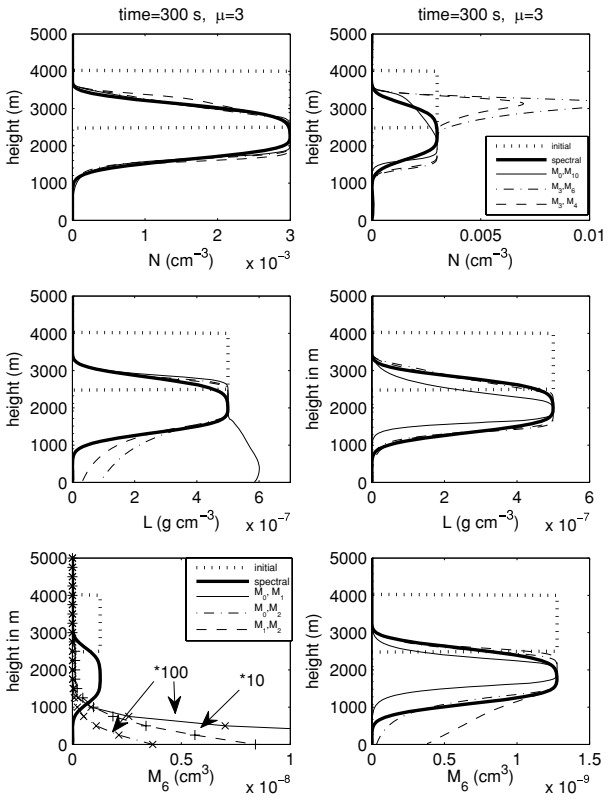


*Fig. 11.* As Fig. 7, but for $\mu = 3$. Note that the $M_6$-values for the $M_0M_1$- and the $M_0M_2$-models are to be multiplied by 100 ('×'), and for the $M_1M_2$-model by 10 ('+').

the flux $F_3$ (and hence $RR$) from $M_0$ and $M_6$. Due to $j = 0 < 3$, $3 + \beta < k = 6$, the profiles of $M_3$ and $F_3$ are considerably damped, see Fig. 6 for $L(z, t)$, and the surface precipitation rate underestimated, see Fig. 8 for $RR(t)$. Another example is model $M_0M_1$. Due to $j = 0$, $k = 1 < 3$, the diagnostic liquid water content $L$ (Fig. 6) and the rain rate $RR$ (Fig. 8) are strongly overestimated, and the sum $L_{\text{int}} + RR_{\text{sum}}$ increases with time well beyond its initial value. Such an extreme violation of mass conservation is intolerable from the physical point of view. Whether the slight change in $L_{\text{int}} + RR_{\text{sum}}$ as in the $M_1M_2$-model is acceptable, should be discussed in the frame of pros and cons for that model.

So far all numerical results hold for a shape parameter $\mu = 0$ in this section. According to the discussion in Section 2 (see Fig. 2) and in Section 3 (see Fig. 5) on the influence of $\mu$, we again expect for increasing $\mu$ a weaker influence of the choice on the prognostic moments $M_j$ and $M_k$ of the evolution of a moment $M_l$. This is indeed confirmed by the results presented in Figs. 10 and 11, which give the vertical distributions of $N$, $L$ and $M_6$ for the same conditions as in Figs. 6 and 7, except for $\mu = 3$. The simulated profiles of $N$, $L$ and $M_6$ from the 2-moment models are closest to the results from the reference model, whenever $l$ is close or equal to one of the orders $j$ or $k$ of the prognostic moments. On the other hand, the $M_0M_3$-model gives a strong overshooting in the profile of the reconstructed moment $M_6$, that is, for $j, k < l$, and the $M_3M_6$- and the $M_3M_4$-models show an overshooting in the $N$-profile, see upper right-hand graph in Fig. 11. These effects are less pronounced than in the case $\mu = 0$. Whenever a bulk model $M_jM_k$ with $\mu = 0$ overestimates (underestimates) precipitation in comparison to the spectral model, it will do so in case of $\mu = 3$ (Fig. 8, right-hand column). Again, the differences are weaker. Thus, the choice of the prognostic moments $M_j$ and $M_k$ becomes less important with increasing $\mu$.

## 5. Discussion and conclusions

Raindrop sedimentation has been simulated using well-known 1-moment and 2-moment parametrization schemes, as well as a spectral microphysical model to provide a reference solution. The parametrization models are based on the assumptions, that the rain drop size distribution and thus the microphysical state is fully determined by one and two parameters, and that these parameters can be uniquely expressed in terms of the selected prognostic moments, which are the moment $M_k$ of order $k$ in case of a 1-moment model and the moments $M_j$ and $M_k$ of order $j$ and $k$, respectively, in case of a 2-moment model. So far, one is free

to choose the prognostic moment(s), since the evolution of each moment is governed by the budget eq. (8). Any other moment $M_l$ then uniquely follows diagnostically from the prognostic moment(s). For practical application, however, the choice of the prognostic moment(s) will have to account for constraints, as discussed below.

The two questions raised in the Introduction are answered now for the sedimentation problem on the basis of the results presented in the preceding sections. First, the evolution of the profile of a moment $M_l(z, t)$ is indeed strongly affected by the selected order of the prognostic moments(s). This is due to the dependence of a drop's sedimentation velocity on its size. As a consequence, the larger the order of a prognostic moment $M_k$, the stronger is the sedimentation flux $F_k$ biased towards the influence of the large particles in the integral (A3). Also the moment-weighted sedimentation velocity $\overline{v}_k$ (A6) increases with the order $k$ of the moment, see Fig. 3. Hence, a prognostic moment of high order will propagate faster downward than a prognostic moment of lower order.

The impact of the selected order of the prognostic moment(s) on the evolution of a diagnostic moment $M_l$ is different in the 1-moment and 2-moment models. In case of the 1-moment model, $M_l$ is diagnosed from the forecasted profile $M_k(z, t)$ and thus will always show the same vertical structure as $M_k$. In particular, the height $z_k$ of the maximum in the $M_k$-profile at time $t$ is determined by $\overline{v}_k$, and the maximum of diagnosed $M_l$ is found at exactly the same height $z_k$ for whatever $l$.

Matters are different for the 2-moment model. Let $z_j$, $z_k$ denote the heights of the maxima in the vertical profiles of the prognostic moments $M_j$, $M_k$. For any $M_jM_k$-model, the heights $z_j$ and $z_k$ differ, as seen in Figs. 6, 7, 10 and 11. Let us define $z_l^*$ as the height of the maximum in the profile of a diagnosed moment $M_l = M_l(M_j, M_k)$. This $z_l^*$ differs from $z_j$ and $z_k$ for $l \neq j, k$. In particular, we find (i) $z_l^* > z_j, z_k$ if $l < j, k$, (ii) $z_j > z_l^* > z_k$ if $j < l < k$ and (iii) $z_l^* < z_k, z_j$ if $j, k < l$. In cases (i) and (iii) an overshooting may be observed, as discussed in Section 4. Furthermore, different profiles of $M_l$ will follow for different combinations $j$ and $k$, as seen in Figs. 6 and 7.

In the previous sections also the sensitivity of the forecasted moments on the shape parameter $\mu$ of the drop size distribution has been inspected. With increasing $\mu$ an integral moment becomes more and more dominated by the contributions from a particular size interval, see Fig. 1. Thus the deviation between the moment-weighted sedimentation velocities, for example, $\overline{v}_j$ and $\overline{v}_k$, of different moments $M_j$ and $M_k$ decreases with increasing $\mu$, so that the choice of the prognostic moments becomes less important. If justified by information on the typical rain drop size distribution, a large $\mu$-value should be used to reduce the influence of the choice of the prognostic moments.

Secondly, there is the question, which moments should be forecasted, when the parametrization is applied in weather prediction and climate models. We start the discussion with the case that only sedimentation influences the drop size spectrum and its moments. The comparison between the results from the spectral resolving reference model and the 1-moment model (Figs. 4 and 5) suggests to choose the prognostic moment to be the physically most relevant one. In case of indecision, a moment of low order is preferable, since the propagation of a moment of high order due to sedimentation is overestimated. The comparison of the results from the reference model and the 2-moment models (Figs. 6 and 11) suggests to predict the moments $M_j$ and $M_k$ such that any moment $M_l$ required in the prediction model is in the range of $j$ and $k$ to prevent overshooting. Unfortunately, this condition cannot be exactly achieved, since the sedimentation flux is proportional to a higher order moment, $F_k \propto M_l$ with $l = k + \beta$. Forecast of prognostic moment $M_{k+\beta}$ is not a solution, because now we have to account for the sedimentation flux $F_{k+\beta} \propto M_{k+2\beta}$.

Furthermore, the orders $j$ and $k$ should not differ too much to avoid strong damping of the profiles of $M_l$ for $j < l < k$, see for example, Fig. 6 for the reconstructed profile of liquid water $L(\propto M_3)$ from the $M_0M_6$-model.

Another criterion for the selection of the prognostic moments is the fulfilment of conservation conditions. While we have the conservative properties for each moment (eq. 9), 1- and 2-moment models can comply with only one and two, respectively, of the conditions as implication of the parametrization assumptions. For instance, conservation of liquid water mass is satisfied only, if $M_3$ (or $L$) is a prognostic moment, see Fig. 9 for the 2-moment model.

The 6th moment, that is radar reflectivity, is relevant, since observation data are frequently available. These data are often used for verification of model results, either by inferring rain rate from observed reflectivity or by diagnosing $M_6$ from the model predicted moment(s). For the 1-moment scheme, the model forecasted $M_6$-profile has the identical vertical structure as the prognostic moment $M_k$. If $k$ is chosen to give best agreement for, for example, $N$- or $L$-profiles with the reference solution, then the diagnosed $M_6$-profile is not a good approximation to the corresponding reference profile. For the 2-moment scheme, the selection of $M_j$ and $M_k$ with $j, k < 6$ gives dubious values for the diagnosed $M_6$-profile, see Fig. 6 for the $M_0M_3$-model. Hence, a verification of model results against observed radar reflectivity cannot give much evidence, since it does not tell much on the quality of other modelled, physically more relevant properties such as, for example, rain rate and liquid water content.

In NWP and climate models, the parametrization scheme has to account also for other cloud physical processes besides sedimentation, such as condensation/evaporation and coagulation. The respective rates of change of a prognostic moment $M_k$ due to these processes are formulated on the basis of the spectral description for any $k$ in terms of integrals over the DSD. The integrals turn out to be proportional to moments $M_l$, with $l$ not necessarily equal to $j$ or $k$. Then the calculation of the transformation rate will be subject to the same problems as discussed

for the diagnosis of $M_l$. In practice, one can consider whether particular properties of the cloud processes can be exploited, such as for instance the invariance of drop number concentration during condensation or invariance of rain water mass during self collection of rain drops.

A crucial point in the parametrization is the DSD function. Assumptions are required despite its large natural variability. Tokay et al. (2001) present fitted parameters for the rain drop DSD of the analytic form (7), and the shape parameter turned out to be $\mu = 1$ for their full database. Furthermore, the authors address that the data for the small- and the large-size ends of the spectra are not very reliable. Similarly, Waldvogel (1974) and Willis (1984) concluded from their observation results, that the fitted exponential DSD is uncertain for large drops. These findings give an argument in favour of predicting low order moments in 1-moment and 2-moment models, since they are less affected by the presence of large drops in the assumed DSD.

A note is added on the occurrence of shock waves in the parametrization models. In case of 1-moment models, the shock wave is apparent at the forefront of the downward travelling signal. Precipitation at level $z = 0$ starts abruptly, irrespective of the choice of the prognostic moment $M_k$, while the starting time depends on the order $k$ and the starting time is latest for lowest $k$. In the 2-moment models the shock wave causes an early onset of precipitation at $z = 0$, see Fig. 8. As long as the early precipitation rate is weak, as is the case for, for example, the $M_0M_3$-model, this phase error should be acceptable. For other combinations of the prognostic moments, the passage of the shock wave can result in excessive values of the diagnosed precipitation rate, as for example, in the $M_0M_1$- and $M_0M_2$-models, see Fig. 8. Yet the amplitude of the shock wave can be influenced to some degree by the non-zero minimum values $N_{\min}$ and $L_{\min}$, which are required to avoid mathematical singularities.

In any parametrization model of the type as applied in this study, the forecast of different moments of the drop size distribution function, but otherwise same assumptions, will give different results for a particular moment $M_l$, as long as the sedimentation velocity of a drop increases with its size. This is all the more important, since the falling drops interact with their environment and among themselves by for example, condensation and coagulation, and these effects are parametrized mathematically in terms of the prognostic moments.

## 6. Acknowledgments

The authors gratefully acknowledge the comprehensive and helpful work of the anonymous reviewers.

## Appendix A: Relationships for the 1-moment scheme

We assume that the size distribution function is given by (7) with constant parameters $n_0$ and $\mu$. Then the $k$th moment $M_k$ is a function of $\lambda$ alone,

$$M_k = \int_0^\infty D^k f(D)\,\mathrm{d}D = n_0\Gamma(k+\mu+1)\lambda^{-(k+\mu+1)}. \tag{A1}$$

$\Gamma(\ldots)$ denotes the gamma function. Likewise, $\lambda$ is expressed by the moment $M_k$,

$$\lambda = [n_0\Gamma(k+\mu+1)]^{1/(k+\mu+1)}\, M_k^{-1/(k+\mu+1)}. \tag{A2}$$

The sedimentation flux $F_k$ of the $k$th moment is defined as

$$F_k = \int_0^\infty D^k v_T(D) f(D)\,\mathrm{d}D \tag{A3}$$

and follows with (2) as

$$F_k = \alpha\frac{\Gamma(\beta+k+\mu+1)}{\Gamma(k+\mu+1)}\frac{M_k^{\beta/(k+\mu+1)}}{[n_0\Gamma(k+\mu+1)]^{\beta/(k+\mu+1)}}\, M_k. \tag{A4}$$

The moment-weighted sedimentation velocity $\overline{v}_k$ is given by

$$\begin{aligned}\overline{v}_k &= \frac{F_k}{M_k} = \alpha\frac{\Gamma(\beta+k+\mu+1)}{\Gamma(k+\mu+1)}\lambda^{-\beta}\\ &= \alpha\frac{\Gamma(\beta+k+\mu+1)}{\Gamma(k+\mu+1)}\frac{M_k^{\beta/(k+\mu+1)}}{[n_0\Gamma(k+\mu+1)]^{\beta/(k+\mu+1)}},\end{aligned} \tag{A5}$$

and the apparent advection velocity $\tilde{v}_k$ follows as

$$\begin{aligned}\tilde{v}_k &= \frac{\mathrm{d}F_k}{\mathrm{d}M_k} = \alpha\frac{\Gamma(\beta+k+\mu+1)}{\Gamma(k+\mu+1)}\frac{\beta+k+\mu+1}{k+\mu+1}\\ &\quad\times\frac{M_k^{\beta/(k+\mu+1)}}{[n_0\Gamma(k+\mu+1)]^{\beta/(k+\mu+1)}}\\ &= \frac{\beta+k+\mu+1}{k+\mu+1}\,\overline{v}_k\,.\end{aligned} \tag{A6}$$

The $l$th moment follows as function of $M_k$ by using $\lambda$ from (A2):

$$\begin{aligned}M_l &= n_0\Gamma(l+\mu+1)\lambda^{-(l+\mu+1)}\\ &= n_0\Gamma(l+\mu+1)\left[\frac{M_k}{n_0\Gamma(k+\mu+1)}\right]^{(l+\mu+1)/(k+\mu+1)}\end{aligned} \tag{A7}$$

Similarly, the moment-weighted sedimentation velocity $\overline{v}_l = F_l/M_l$ and the apparent advection velocity $\tilde{v}_l = \mathrm{d}F_l/\mathrm{d}M_l$ of the $l$th moment are related to $\overline{v}_k$ and $\tilde{v}_k$, respectively, by

$$\overline{v}_l = \frac{\Gamma(k+\mu+1)}{\Gamma(l+\mu+1)}\frac{\Gamma(\beta+l+\mu+1)}{\Gamma(\beta+k+\mu+1)}\,\overline{v}_k \tag{A8}$$

$$\tilde{v}_l = \frac{\Gamma(k+\mu+2)}{\Gamma(l+\mu+2)}\frac{\Gamma(\beta+l+\mu+2)}{\Gamma(\beta+k+\mu+2)}\,\tilde{v}_k. \tag{A9}$$

Suppose $l > k$. Since $\beta > 0$, it follows that

$$\begin{aligned}\overline{v}_l &= \frac{\Gamma(k+\mu+1)}{(l+\mu)(l+\mu-1)\ldots(k+\mu+1)\Gamma(k+\mu+1)}\\ &\quad\times\frac{(\beta+l+\mu)\ldots(\beta+k+\mu+1)\Gamma(\beta+k+\mu+1)}{\Gamma(\beta+k+\mu+1)}\,\overline{v}_k\\ &= \frac{(\beta+l+\mu)\ldots(\beta+k+\mu+1)}{(l+\mu)\ldots(k+\mu+1)}\,\overline{v}_k \;>\; \overline{v}_k,\end{aligned} \tag{A10}$$

$$\tilde{v}_l = \frac{\Gamma(k+\mu+2)}{(l+\mu+1)(l+\mu)\dots(k+\mu+2)\Gamma(k+\mu+2)} \times \frac{(\beta+l+\mu+1)\dots(\beta+k+\mu+2)\Gamma(\beta+k+\mu+2)}{\Gamma(\beta+k+\mu+2)}\,\tilde{v}_k = \frac{(\beta+l+\mu+1)\dots(\beta+k+\mu+2)}{(l+\mu+1)\dots(k+\mu+2)}\,\tilde{v}_k \;>\; \tilde{v}_k. \quad \text{(A11)}$$

Likewise one can show for $l < k$ that $\overline{v}_l < \overline{v}_k$ and $\tilde{v}_l < \tilde{v}_k$.

## Appendix B: Relationships for the 2-moment scheme

We assume the size distribution function is given by (7) as in Appendix A, however, now with the single constant parameter $\mu$. Any moment follows as function of the parameters $\lambda$ and $n_0$, see (A1). We can express $\lambda$ and $n_0$ as functions of the two moments $M_j$ and $M_k$

$$\lambda = \left[\frac{M_j}{M_k}\frac{\Gamma(k+\mu+1)}{\Gamma(j+\mu+1)}\right]^{1/(k-j)} \quad \text{(B1)}$$

$$n_0 = \left[\frac{M_j}{\Gamma(j+\mu+1)}\right]^{(k+\mu+1)/(k-j)} \times \left[\frac{M_k}{\Gamma(k+\mu+1)}\right]^{-(j+\mu+1)/(k-j)}. \quad \text{(B2)}$$

Without lack of generality, we use $j < k$ everywhere.

The sedimentation fluxes $F_j$ and $F_k$ are calculated from (A3) with (2). Replacing the parameters $\lambda$ and $n_0$ in terms of the two moments $M_j$ and $M_k$, we find the fluxes

$$F_j = \alpha\,\Gamma(\beta+j+\mu+1) \times \left[\frac{M_k}{\Gamma(k+\mu+1)}\right]^{\beta/(k-j)} \left[\frac{M_j}{\Gamma(j+\mu+1)}\right]^{-(\beta+j-k)/(k-j)} \quad \text{(B3)}$$

$$F_k = \alpha\,\Gamma(\beta+k+\mu+1) \times \left[\frac{M_k}{\Gamma(k+\mu+1)}\right]^{(\beta+k-j)/(k-j)} \left[\frac{M_j}{\Gamma(j+\mu+1)}\right]^{-\beta/(k-j)}. \quad \text{(B4)}$$

The moment-weighted sedimentation velocities then read

$$\overline{v}_j = \frac{F_j}{M_j} = \alpha\frac{\Gamma(\beta+j+\mu+1)}{\Gamma(j+\mu+1)}\lambda^{-\beta} = \alpha\,\frac{\Gamma(\beta+j+\mu+1)}{\Gamma(j+\mu+1)}\left[\frac{M_k}{M_j}\frac{\Gamma(j+\mu+1)}{\Gamma(k+\mu+1)}\right]^{\beta/(k-j)} \quad \text{(B5)}$$

$$\overline{v}_k = \frac{F_k}{M_k} = \alpha\frac{\Gamma(\beta+k+\mu+1)}{\Gamma(k+\mu+1)}\lambda^{-\beta} = \alpha\,\frac{\Gamma(\beta+k+\mu+1)}{\Gamma(k+\mu+1)}\left[\frac{M_k}{M_j}\frac{\Gamma(j+\mu+1)}{\Gamma(k+\mu+1)}\right]^{\beta/(k-j)}. \quad \text{(B6)}$$

$\overline{v}_j$ and $\overline{v}_k$ differ only by a constant factor, and for $j < k$ we find

$$\overline{v}_j = \frac{\Gamma(\beta+j+\mu+1)}{\Gamma(\beta+k+\mu+1)}\frac{\Gamma(k+\mu+1)}{\Gamma(j+\mu+1)}\,\overline{v}_k = \frac{(k+\mu)\dots(j+\mu+1)}{(\beta+k+\mu)\dots(\beta+j+\mu+1)}\,\overline{v}_k \;<\; \overline{v}_k. \quad \text{(B7)}$$

As for the one-moment scheme, the moment-weighted sedimentation velocity increases with increasing order of the moment. Note that $\overline{v}_k$ according to (A5) for the 1-moment model and to (B6) for the 2-moment model are expressed by the same functional relationship. For given $\lambda$ as function of prescribed $L$ and $N$, as used for Fig. 3, the results for $\overline{v}_k$ coincide in both models.

The $l$th moment follows in terms of the prognostic moments $M_j$ and $M_k$ from (A1), (B1) and (B2) as

$$M_l = \Gamma(l+\mu+1) \times \left[\frac{M_k}{\Gamma(k+\mu+1)}\right]^{(l-j)/(k-j)} \left[\frac{M_j}{\Gamma(j+\mu+1)}\right]^{(k-l)/(k-j)}, \quad \text{(B8)}$$

and the sedimentations flux $F_l$ follows as

$$F_l = \alpha\,\Gamma(\beta+l+\mu+1) \times \left[\frac{M_k}{\Gamma(k+\mu+1)}\right]^{(\beta+l-j)/(k-j)} \left[\frac{M_j}{\Gamma(j+\mu+1)}\right]^{(k-l-\beta)/(k-j)}. \quad \text{(B9)}$$

The moments may generally become also zero. Then singularities for $M_l$ arise if $j > l$ or if $k < l$, according to the diagnostic eq. (B8). To avoid such singularities, we prescribe non-zero minimum values $N_{\min}$ and $L_{\min}$, from which also the minima of the other moments are derived. $N_{\min} = 10^{-12}$ cm$^{-3}$ and $L_{\min} = 10^{-17}$ g cm$^{-3}$ are used for the examples presented in this study.

## References


Collins, W. D., Rasch, P. J., Boville, B. A. and co-authors. 2004. Description of the NCAR Community Atmosphere Model (CAM 3.0). *NCAR Technical Note* **TN-464+STR**, http://www.ccsm.ucar.edu/models/atm-cam.

Doms, G., Förstner, J., Heise, E. and co-authors 2003. *A Description of the Nonhydrostatic Regional Model LM*. Consortium for Small Scale Modelling (COSMO), http://cosmo-model.cscs.ch/content/model/documentation/core/default.htm.

Geleyn, J.-F., Catry, B., Bouteloup, Y. and Brozkova, R. 2008. A statistical approach for sedimentation inside a microphysical precipitation scheme. *Tellus* **60A**, 649–662.

Ferrier, B. S. 1994. A double-moment multiple-phase four-class bulk ice scheme: Part I: description. *J. Atmos. Sci.* **51**, 249–280.

Kessler, E. 1969. *On the Distribution and Continuity of Water Substance in Atmospheric Circulations*. Amer. Meteor. Soc., Boston.

Khain, A., Pokrovsky, A., Pinsky, M., Seifert, A. and Phillips, V. 2004. Simulations of effects of atmospheric aerosols on deep turbulent convective clouds by using a spectral microphysics mixed-phase

cumulus cloud model. Part I: model description and possible applications. *J. Atmos. Sci.* **61**, 2963–2982.

Lüpkes, C., Beheng, K. B. and Doms, G. 1989. A parameterization scheme for simulating collision/coalescence of water drops. *Beitr. Phys. Atmos.* **62**, 289–306.

Lynn, B. and Khain, A. 2007. Utilization of spectral bin microphysics and bulk parameterization schemes to simulate the cloud structure and precipitation in a mesoscale rain event. *J. Geophys. Res.* **112**, D22205, DOI: 10.1029/2007JD008475.

Lynn, B., Khain, A., Dudhia, J. and co-authors 2005. Spectral (bin) microphysics coupled with a mesoscale model (MM5). Part I: model description and first results. *Mon. Wea. Rev.* **133**, 44–58.

Milbrandt, J. A. and Yau, M. K. 2005a. A multimoment bulk microphysics parameterization. Part I: analysis of the role of the spectral shape parameter. *J. Atmos. Sci.* **62**, 3051–3064.

Milbrandt, J.A. and Yau, M. K. 2005b. A multimoment bulk microphysics parameterization. Part II: a proposed three-moment closure and scheme description. *J. Atmos. Sci.* **62**, 3065–3081.

Roeckner, E., Bäuml, G., Bonaventura, L. and co-authors 2003. The atmospheric general circulation model ECHAM5. Part. *Max Planck Institute for Meteorology* **Report No. 349**, http://www.mpimet.mpg.de/en/wissenschaft/modelle/echam/echam5.html#c2782.

Saito, K., Fujita, T., Yamada, Y. and co-authors 2006. The operational JMA nonhydrostatic mesoscale model. *Mon. Wea. Rev.* **134**, 1266–1298.

Seifert, A. and Beheng, K. D. 2005. A two-moment cloud microphysics parameterization for mixed-phase clouds. Part I: model description. *Meteorol. Atmos. Phys.* **92**, 45–66.

Tokay, A., Kruger, A. and Krajewski, W. F. 2001. Comparison of drop size distribution measurements by impact and optical disdrometers. *J. Appl. Meteor.* **40**, 2083–2097.

Toro, E. F. 1999. *Riemann Solvers and Numerical Methods for Fluid Dynamics*. Springer, Berlin.

Wacker, U. and Seifert, A. 2001. Evolution of rain water profiles resulting from pure sedimentation: spectral vs. parameterized description. *Atmos. Res.* **58**, 19–39.

Waldvogel, A. 1974. The $N_0$ jump of raindrop spectra. *J. Atmos. Sci.* **31**, 1067–1078.

Willis, P. 1984. Functional fits to some observed drop size distributions and parameterization of rain. *J.Atmos. Sci.* **41**, 1648–1661.